

MIT Open Access Articles

Baroclinic Eddy Equilibration under Specified Seasonal Forcing

The MIT Faculty has made this article openly available. **Please share** how this access benefits you. Your story matters.

Citation: Zhang, Yang, Peter H. Stone, 2010: Baroclinic Eddy Equilibration under Specified Seasonal Forcing. *J. Atmos. Sci.*, 67, 2632–2648. © 2010 American Meteorological Society.

As Published: <http://dx.doi.org/10.1175/2010jas3392.1>

Publisher: American Meteorological Society

Persistent URL: <http://hdl.handle.net/1721.1/62600>

Version: Final published version: final published article, as it appeared in a journal, conference proceedings, or other formally published context

Terms of Use: Article is made available in accordance with the publisher's policy and may be subject to US copyright law. Please refer to the publisher's site for terms of use.



Baroclinic Eddy Equilibration under Specified Seasonal Forcing

YANG ZHANG

School of Atmospheric Sciences, Nanjing University, Nanjing, China

PETER H. STONE

EAPS, Massachusetts Institute of Technology, Cambridge, Massachusetts

(Manuscript received 30 November 2009, in final form 22 March 2010)

ABSTRACT

Baroclinic eddy equilibration under a Northern Hemisphere–like seasonal forcing is studied using a modified multilayer quasigeostrophic channel model to investigate the widely used “quick baroclinic eddy equilibration” assumption and to understand to what extent baroclinic adjustment can be applied to interpret the midlatitude climate. Under a slowly varying seasonal forcing, the eddy and mean flow seasonal behavior is characterized by four clearly divided time intervals: an eddy inactive time interval in summer, a mainly dynamically determined eddy spinup time interval starting in midfall and lasting less than one month, and a quasi-equilibrium time interval for the zonal mean flow available potential energy from late fall to late spring, with a mainly external forcing determined spindown time interval for eddy activity from late winter to late spring. The baroclinic adjustment can be clearly observed from late fall to late spring. The sensitivity study of the eddy equilibration to the time scale of the external forcing indicates that the time scale separation between the baroclinic adjustment and the external forcing in midlatitudes is only visible for external forcing cycles one year and longer.

In spite of the strong seasonality of the eddy activity, similar to the observations, a robust potential vorticity (PV) structure is still observed through all the seasons. However, it is found that baroclinic eddy is not the only candidate mechanism to maintain the robust PV structure. The role of the boundary layer thermal forcing and the moist convection in maintaining the lower-level PV structure is discussed. The adjustment and the vertical variation of the lower-level stratification play an important role in all of these mechanisms.

1. Introduction

The Northern and Southern Hemispheres have different seasonality in surface temperature, atmospheric temperature, and eddy activities (Trenberth 1991; Peixoto and Oort 1992; Zhang 2009), with the Northern Hemisphere atmosphere exhibiting much stronger seasonal variation in midlatitudes. In spite of the strong seasonal variation of the atmospheric flow, observations indicate that the isentropic slope (Stone 1978) and the potential vorticity (PV) gradient (Kirk-Davidoff and Lindzen 2000) in the midlatitudes show little variation through all the seasons. This raises questions as to how to interpret the robust PV structure or, more specifically, as to whether the robustness of the PV structure indicates any

dynamic constraints. To answer these questions, several theories have been proposed. One of them, which has attracted considerable attention, is baroclinic adjustment, which was first clearly proposed by Stone (1978) and further studied by Gutowski (1985), Cehelsky and Tung (1991), Lindzen (1993), and Zurita and Lindzen (2001). Baroclinic adjustment suggested a tendency of the baroclinic eddies to homogenize the mean flow PV gradient and proposed a preferred equilibrium state as well as a strong feedback between the eddy heat fluxes and the temperature structure. In the baroclinic adjustment scenario, the eddy fluxes are sensitive to the variation of the external forcing (i.e., seasonal forcing and climate change) but the structure of the mean state is left almost unchanged or only slightly changed.

Although the concept of baroclinic adjustment was partly inspired by the observed extratropical robust isentropic slope and PV structure through all the seasons, baroclinic eddy equilibration under a time-varying

Corresponding author address: Yang Zhang, 22 Hankou Road, Nanjing, Jiangsu 210093, China.
E-mail: yangzh@alum.mit.edu

seasonal forcing is barely studied. Instead, many equilibrium studies have been carried out to investigate the baroclinic adjustment (Stone and Branscome 1992; Welch and Tung 1998a,b; Solomon and Stone 2001b; Zurita-Gotor 2008, etc.), in which the external forcing is always specified and kept fixed during the eddy equilibration. These studies investigated the factors that determine the equilibrium state and showed that when the external forcing is a slow process compared to the baroclinic eddies, in equilibrium a robust PV structure can always be maintained in spite of the changes in the external forcing. Then how can these results be applied to interpret the observed midlatitude climate? The answer is based on the validity of one commonly used assumption on the baroclinic eddy equilibration time scale (or baroclinic adjustment time scale), in which the mean flow adjustment by the baroclinic eddies is always assumed to be much faster than the variation of the external forcing. If this assumption is appropriate, the conclusions from the equilibrium studies can be used to interpret and predict the midlatitude climate by assuming that in spite of the variation of the external forcing, the baroclinic eddies can always quickly respond to the variation and adjust the mean flow to an equilibrium state. This time scale assumption is a precondition that baroclinic adjustment theories work well in the real atmosphere.

However, as suggested in Zurita-Gotor and Lindzen (2007), an estimate of the baroclinic adjustment time scale is not easy, and the time scale separation between the dynamics and the external forcing is not clear in midlatitudes. If the eddy growth rate predicted by the baroclinic instability is relevant to estimate the adjustment time scale, a time scale of a few days would be suggested, which is also the life cycle time scale of synoptic eddies in midlatitudes. The eddy–mean flow interaction, however, usually takes a longer time. Many numerical studies suggest that the equilibration of the baroclinic eddies is much longer than a single life cycle and can be as long as 100 days (Solomon and Stone 2001a; Chen et al. 2007). In addition, the boundary layer forcing, as suggested by Swanson and Pierrehumbert (1997) and further studied by Zhang et al. (2009), acts on the surface air in less than one day, which is a faster process than the baroclinic eddies. Above the boundary layer, the radiative forcing time scale, which is around tens of days, is slower than the baroclinic eddies, but the moist convection and release of latent heating, which may also play an important role in midlatitudes (Emanuel 1988; Gutowski et al. 1992; Juckes 2000; Korty and Schneider 2007), can be a fast process. The time scale of the baroclinic adjustment was explicitly addressed by Barry et al. (2000). In the spin-down experiment using a general circulation model by turning off the radiation and other physical processes,

a 15–20-day adjustment time scale for the temperature and a roughly 30-day adjustment time scale for the stratification were suggested, which is comparable with the radiative time scale and questions the validity of the baroclinic adjustment.

In this study, we want to test the quick baroclinic eddy adjustment assumption by studying the baroclinic eddy equilibration under a time-varying external forcing. The example of the time-varying forcing we choose is the Northern Hemisphere–like seasonal forcing, in which the surface temperature is specified to vary seasonally to act on the atmospheric flow through the boundary layer processes and the radiative–convective heating. We hope our study can help elucidate to what extent the quick adjustment time scale can be a good assumption when applied to the real atmosphere and to what extent the baroclinic adjustment theory can be applied to interpret the robust thermal structure in the Northern Hemisphere midlatitudes.

Our numerical studies of the baroclinic eddy equilibration under the specified seasonal forcing find that under the slowly varying seasonal forcing, the eddy and the mean flow behavior can be clearly divided into four time intervals: an eddy inactive time interval in summer, a mainly dynamically determined eddy spinup time interval starting in midfall and lasting less than one month, and a “quasi-equilibrium” time interval for the zonal mean flow available potential energy from late fall to late spring, with a mainly external forcing determined eddy spindown time interval from late winter to late spring. The baroclinic adjustment scenario only occurs in the quasi-equilibrium time interval. In spite of the strong seasonality of the eddy activity, a robust PV structure is still observed through all the seasons. Baroclinic eddies are able to maintain a robust PV structure, especially during the winter. However, it is not the only possible mechanism. Boundary layer thermal forcing can maintain a robust lower-level PV structure by strongly modifying the lower-level stratification. The vertical variation of the moist adiabatic lapse rate can also affect the PV structure. Our sensitivity study of the eddy equilibration to the time scale of the external forcing also indicates that the time scale separation between the baroclinic adjustment and the external forcing in midlatitudes is only visible for external forcing cycles one year and longer.

The structure of this paper is as follows. The model and the seasonal forcing setups are described in section 2. The seasonal behavior of the eddy and the mean flow under a Northern Hemisphere–like seasonal forcing is shown in section 3. Interpretations of the robust PV structure through all the seasons and the role of baroclinic eddies, boundary layer thermal forcing, and moist convection in maintaining the robust PV structure are discussed in

section 4. The validity of the quick baroclinic adjustment assumption is investigated in section 5 by carrying out sensitivity studies on the time scale of the seasonal forcing, in which the factors determining the eddy seasonal behavior are also discussed. A summary and discussion of the results are presented in section 6.

2. Experiment description

In this study, seasonal behavior of the atmospheric flow is investigated using a β -plane multilevel quasigeostrophic (QG) channel model with interactive static stability and a simplified parameterization of atmospheric boundary layer physics, similar to that of Solomon and Stone (2001a,b) and Zhang et al. (2009) (see the appendix for details of the model). The model has a channel length of 21 040 km, which is comparable to the length of the latitudinal belt in midlatitudes, and a channel width of 10 000 km with the baroclinic zone centered over the central half of the channel. A rigid lid is added at the top as the boundary condition.

Seasonal forcing is applied to the atmospheric flow through the seasonally varying lower boundary condition and the radiative–convective heating. In the experiments, seasonal variation of the underlying surface temperature T_g is specified as the lower boundary condition. The surface temperature anomaly T_g^\dagger [where $T_g^\dagger = T_g - \overline{T}_g^{xy}$, and $(\overline{\cdot})^{xy}$ means horizontal average] is set to vary as

$$T_g^\dagger(y, t) = -\frac{\Delta T_g(t)}{2} \sin\left[\frac{\pi(y - L/2)}{L/2}\right] \quad (1)$$

over the central half of the channel, which is $1/4L \leq y \leq 3/4L$, where L is the width of the channel. There is no meridional temperature gradient in regions $0 \leq y \leq 1/4L$ and $3/4L \leq y \leq L$. In the standard run (SD run) experiment, the surface temperature difference over the central half of the channel ΔT_g is specified to vary periodically with time t as the observed seasonal variation of the surface air potential temperature difference between 20° and 70°N . Thus, as shown in Fig. 1, the surface temperature varies seasonally with the north–south temperature difference over the channel, being as large as 43 K in winter and as weak as 18 K in summer. Since in our QG model the baroclinicity of the surface temperature is the main factor that influences the baroclinic eddy activity in the atmosphere, the seasonal variation of \overline{T}_g^{xy} is not considered.

In addition to the boundary layer processes, seasonal variation of the surface temperature is further “felt” by the atmospheric flow through the radiative–convective heating. As discussed in the appendix, the radiative–convective heating is parameterized by the Newtonian

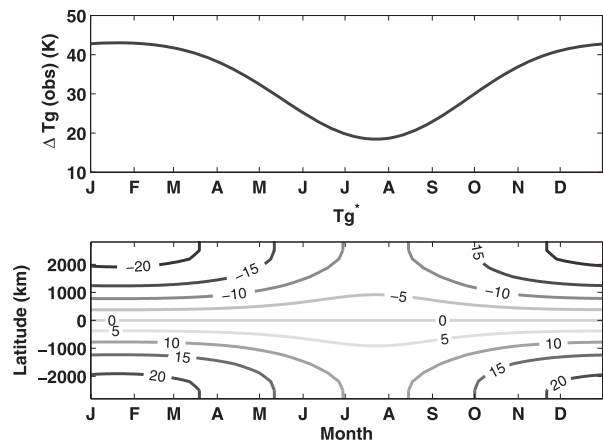


FIG. 1. (top) Seasonal variation of the 20° – 70°N surface air potential temperature difference calculated using NCEP–NCAR reanalysis data from year 1967 to 2007, which is also the seasonal variation of ΔT_g used in the model; (bottom) seasonal variation of the surface temperature anomalies over the central half of the channel used in the model, where the plotted contour interval is 5 K.

cooling form, with a relaxation time of 40 days. The target state potential temperature θ_e , where

$$\theta_e(y, p, t) = \theta_e^\dagger(y, p, t) + \overline{\theta}_e^{xy}(p, t), \quad (2)$$

is also specified to vary seasonally to match the underlying surface temperature. In the model, we assume that θ_e^\dagger has the same meridional distribution as T_g^\dagger in the troposphere. Above 250 hPa, which is above the tropopause, an isothermal stratosphere is included in the model.

As discussed in Zhang et al. (2009), one important difference between this model and traditional QG models is that the horizontally averaged potential temperature and static stability, instead of being specified, are allowed to evolve with time. In this study, the target state temperature lapse rate also includes seasonal variations. The study by Stone and Carlson (1979) showed that the stratification in the midlatitudes in the Northern Hemisphere exhibits strong seasonal variation, especially when compared with the moist adiabatic lapse rate. As shown in Figs. 2a and 2b, the stratification in the midlatitudes is close to the moist adiabatic rate in summer but much more stable than the moist adiabatic lapse rate in winter, which is attributed to the stabilization by baroclinic eddies. As suggested by Schneider (2007), the adjustment of the stratification by baroclinic eddies may play an important role in maintaining the robust isentropic slope in the midlatitudes. Thus (as displayed in Fig. 2c), in the troposphere the seasonal variation of the moist adiabatic state lapse rate Γ_m is used to represent the radiative–convective

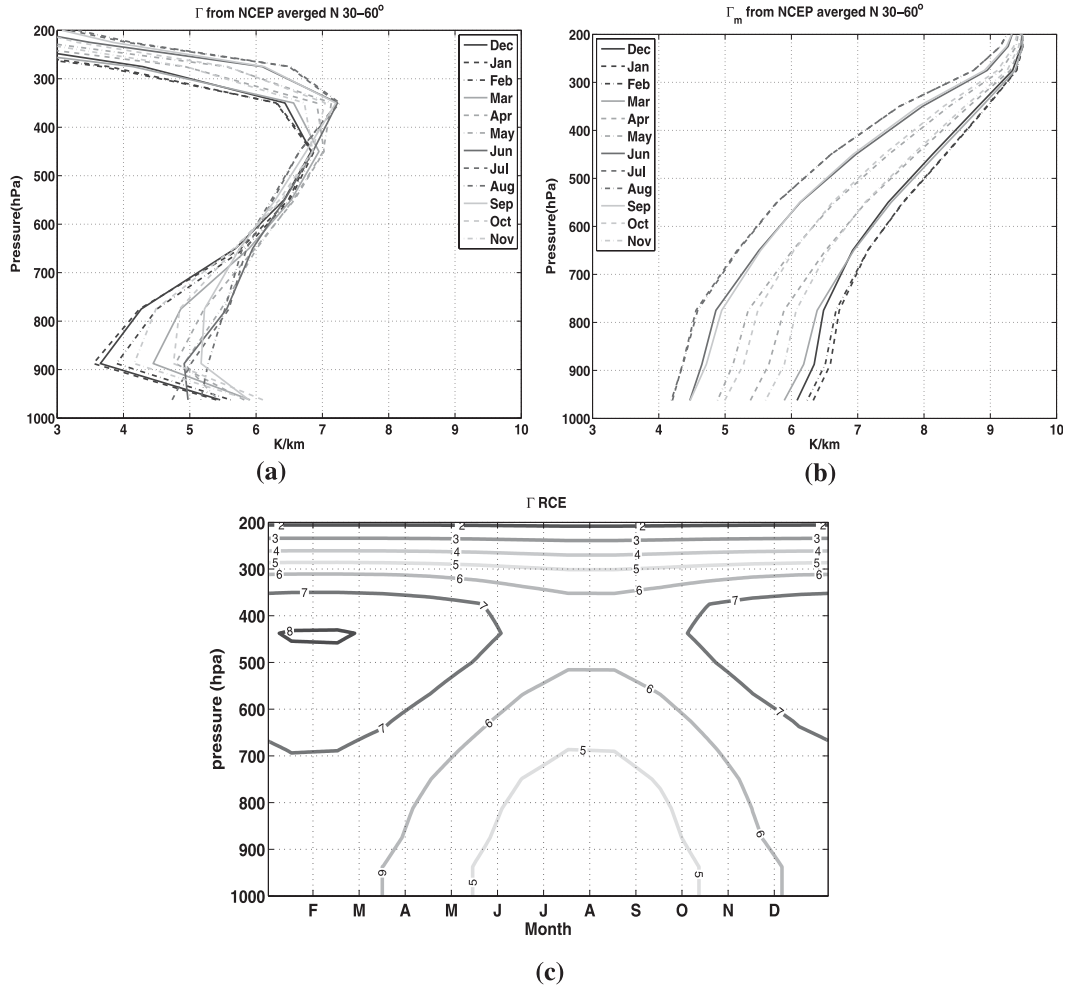


FIG. 2. Vertical distribution of (a) the monthly mean lapse rate and (b) the lapse rate in the moist adiabatic state averaged over the NH midlatitudes (30°–60°N) calculated from NCEP–NCAR reanalysis data, and (c) seasonal variation of the RCE state lapse rate used in the model, where the plotted contour interval is 1 K km⁻¹.

equilibrium (RCE) state lapse rate $-d\bar{T}_e^{xy}/dz$, whose seasonal variation is estimated as in Stone and Carlson (1979) and Schneider (2007). In the stratosphere, we assume that $-d\bar{T}_e^{xy}/dz = 0$ through all the seasons.

3. Standard run

A standard run experiment is carried out to simulate a realistic Northern Hemisphere climate in the midlatitudes. Before the 3D standard run simulation, a 2D (zonal symmetric) simulation is carried out first, in which baroclinic eddies are not presented. Since under the QG framework the 2D flow is weak and mostly confined in the boundary layer (not shown), the thermal structure of the zonal flow is the direct result of the external forcing. As shown in Fig. 3b, compared with the target state temperature gradient at the center of the channel in Fig. 3a,

because of the boundary layer processes the atmospheric flow in the boundary layer can “feel” the seasonal variation immediately, while the flow in the free troposphere varies almost one month later, primarily because of the slow relaxation time scale of the radiative–convective heating.

Under the same external forcing, a 3D standard run simulation is started on 1 January. The zonal symmetric RCE state with the 1 January forcing is set as the initial state and small-amplitude perturbations are added into the system at the initial moment. After running the model for 400 days with fixed external forcing, the flow reaches an equilibrium state. Then we turn on the seasonal variation of the external forcing. Model results show that after running for more than one seasonal cycle, the atmospheric flow exhibits a repeated annual pattern. The standard seasonal experiment is run for 15 yr. The statistics

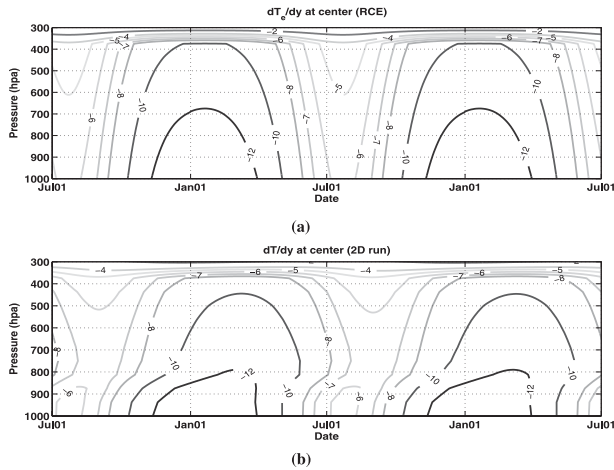


FIG. 3. Time evolution of the meridional temperature gradient [$\text{K} (1000 \text{ km})^{-1}$] at the center of the channel (a) in the RCE state and (b) in the 2D simulation in two seasonal cycles.

shown below are from the model results of the last 10 yr.¹

Seasonal variations of the domain averaged mean available potential energy (MPE), eddy available potential energy (EPE), eddy kinetic energy (EKE), and mean kinetic energy (MKE) are displayed in Fig. 4. Thin curves in these plots show the annual behavior of the energies in each of the 10 yr; the 10-yr mean seasonal variations are plotted with thick black curves. MPE, as in Peixoto and Oort (1992), is defined as

$$\text{MPE} = \frac{c_p}{2} \int \sigma ([T] - \overline{T}^{xy})^2 dm, \quad (3)$$

where

$$\sigma = -\frac{R}{pc_p} \left(\frac{p_0}{p} \right)^{R/c_p} \left(\frac{\partial \overline{\theta}^{xy}}{\partial p} \right)^{-1} \quad (4)$$

is the stratification parameter and $[\cdot \cdot \cdot]$ means zonal average. The definitions of EPE, EKE, and MKE are also the same as in Peixoto and Oort (1992). In Fig. 4a, the seasonal variation of the RCE state MPE is also plotted, which can be considered as an index for the external forcing exerted on the flow and also the source of the seasonality specified in the model. Even though the

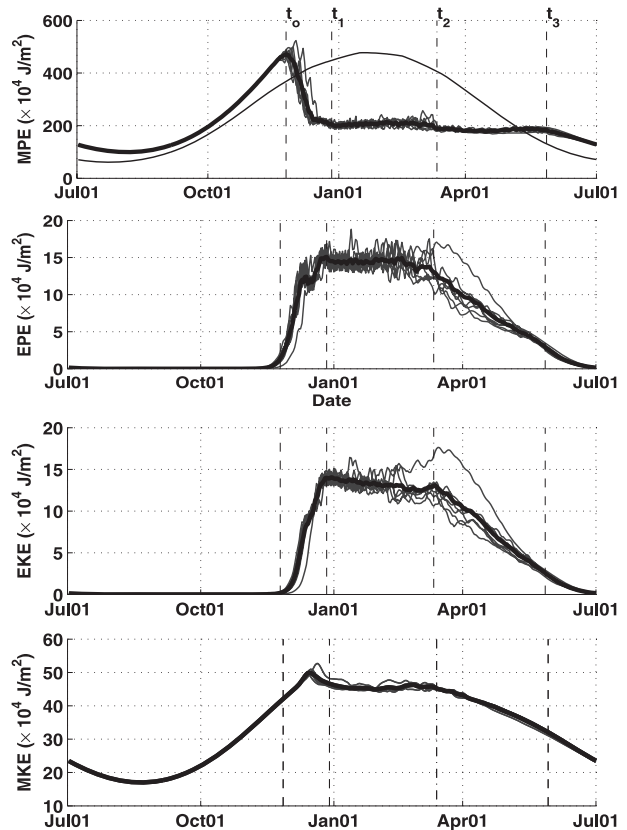


FIG. 4. Seasonal variation of domain averaged (a) MPE, (b) EPE, (c) EKE, and (d) MKE. The thin curves show the energy evolution in each of the last 10 yr. The thick black curve shows the mean seasonal variations of the last 10 yr. In (a), the seasonal evolution of the RCE state MPE is plotted in thin black curve. Units for energy are 10^4 Joules per square meter. Times t_0 , t_1 , t_2 , and t_3 are marked with thin dashed lines.

eddy activities have their own variations year by year (as do the energies in the zonal mean flow), their annual behaviors are highly similar and have robust characteristics, which can be clearly divided into four time intervals. Times t_0 , t_1 , t_2 , and t_3 are used to distinguish these time intervals.

- Model results show that there is almost no significant eddy activity from early summer to late fall. The external forcing, as well as MPE and MKE, is smallest during this period.
- As the differential heating and the MPE increase, eddies begin to spin up. Eddy energies increase almost exponentially in the late fall, while MPE starts to decrease rapidly at t_0 as marked in Fig. 4a, even though the external forcing is still increasing in this period. Around t_1 , MPE stops decreasing, which is also the time when eddy energies reach their maximum values.
- After t_1 , in spite of the variation of external forcing, MPE maintains a quasi-equilibrium state with a

¹ Sensitivity test of the initial condition has been carried out by varying the starting date and the initial state. Model results show that the seasonal behavior of the eddy and the mean flow is insensitive to the setting of the start date and the initial state (Zhang 2009). After the model is run for more than one seasonal cycle, the eddy and the mean flow exhibit similar annual patterns in these runs.

relatively constant value until t_3 . The time interval from t_1 to t_3 is also the period when baroclinic eddies have strong activities with almost exact equipartition between EPE and EKE, which is also found in other dry and moist simulations (e.g., Schneider and Walker 2006; O’Gorman and Schneider 2008) and is consistent with the character of the weakly nonlinear flow (Pedlosky 1970).

- The eddy activity and MKE indicate that the time interval from t_1 to t_3 can be further divided into two parts. From t_1 to t_2 , eddy energies and MKE only have mild variations. Starting from t_2 , eddy energies and MKE decay quickly. At t_3 , the eddy activity is reduced to small values.
- After t_3 , eddies no longer play any significant role in the system and the circulation is similar to that in the 2D simulation. The atmosphere enters an eddy inactive time interval again.

Consistent with the zonal/eddy kinetic and available potential energies, the zonal mean flow also shows obvious seasonal behavior. As shown in Fig. 5a, the temperature gradient at the center of the channel, compared with the 2D symmetric run in Fig. 3b, is greatly reduced as the eddies spin up, especially near 800 hPa, which is also the location of the steering level. During the quasi-equilibrium state from t_1 to t_3 , the temperature gradient above the boundary layer is also maintained at a relatively constant state. After t_3 , the temperature gradient again varies with time and behaves like that in the 2D run.

Seasonal variation of the domain averaged static stability is shown in Fig. 5b. Compared with the target state lapse rate in Fig. 2c, modification of the stratification mainly lies in the lower troposphere. From t_3 to t_0 , when baroclinic eddies are not active, vertical distribution of the domain averaged lapse rate in lower levels shows characteristics of a well-mixed boundary layer (Stull 1988): much less stable stratification in the boundary layer because of the strong vertical thermal diffusion and strongly stable stratification just above the boundary layer (the boundary layer is defined below 850 hPa). From t_0 , as the eddy spins up, the location of the stratification maximum moves down and stays around 870 hPa from t_1 to t_2 . In the eddy decay period, the peak of the stratification slowly moves up.

The time evolution of the PV gradient at the center of the channel is also plotted in Fig. 5c. Despite the strong seasonality of eddy activity, the PV gradient keeps a similar vertical distribution through the whole year, as in the real atmosphere (Kirk-Davidoff and Lindzen 2000). In the eddy spinup time interval, the small PV gradient region moves lower compared with the eddy inactive time

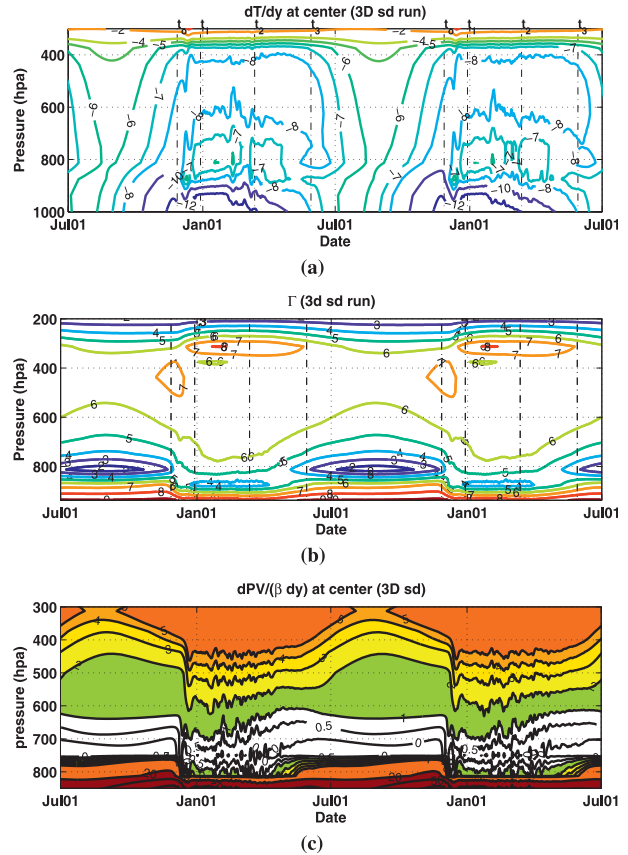


FIG. 5. Time evolution of (a) the meridional temperature gradient [$\text{K} (1000 \text{ km})^{-1}$], (b) lapse rate (K km^{-1}) and (c) the meridional PV gradient at the center of the channel in the SD run in two seasonal cycles. In (c), the PV gradient is normalized with β and the white area indicates regions where the PV gradient is weaker than β .

interval, which, as suggested in Zurita-Gotor and Lindzen (2004), coincides with the dropping of the steering level as the eddies spin up a barotropic jet (results not shown here). In the eddy active time interval, the smallest PV gradient lies around the 800 hPa and slowly moves up as the eddy decays. However, even in the eddy inactive time interval, a weak PV gradient is still observed above the top of the boundary layer. As a result, the PV structure there is relatively robust through the whole year.

4. PV gradient and the role of stratification

In the SD run, just as observed in the Northern Hemisphere midlatitude, the PV structure is robust over all the year. During the winter, when baroclinic eddies are active, the robustness of the PV gradient is consistent with the previous equilibrium studies (Stone and Branscome 1992; Solomon and Stone 2001b; Zurita-Gotor 2008). However, the robust PV structure in the eddy inactive period in our

model indicates that baroclinic eddies may not be the only candidate for the observed PV structure. In this section, we will discuss the possible mechanisms that can maintain the robust PV structure.

In a β -plane QG model, the distribution of the meridional PV gradient, which by definition is

$$\frac{\partial q}{\partial y} = \beta - u_{yy} + f_0 \frac{\partial \theta_y}{\partial p \frac{\partial \theta_y}{\partial y}}, \quad (5)$$

is virtually determined by the distribution of the isentropic slope (since the meridional shear of the zonal wind is always small). Equation (5) shows that if the isentropic slope becomes steeper with height, the baroclinic term will act against β to reduce the PV gradient. Otherwise, the baroclinic term has the same sign as β and acts to enhance the PV gradient (e.g., the strong PV gradient near the tropopause). Baroclinic eddy is known to play an important role in constraining the midlatitude isentrope distribution (Schneider 2004; Zurita-Gotor 2008). In our modified QG model, as shown in Fig. 5, in addition to reducing the meridional temperature gradient as in the traditional QG model, baroclinic eddies can modify the PV gradient by stabilizing the lower troposphere's stratification. During summer, baroclinic eddies are too weak to play any role in the system; therefore, the thermal structure is mainly determined by the radiative–convective heating and the boundary layer forcing.

The role of these processes in determining the PV gradient is further studied below by carrying out groups of sensitivity studies. In the first group of simulations, we carry out the same 2D and 3D runs as in section 3 but with the top of the boundary layer changed from 850 to 700 hPa. In another group of sensitivity studies, two 2D simulations are carried out, in which we assume the RCE state lapse rate is 8 K km^{-1} in the troposphere (which is closer to the dry adiabatic state) and isothermal in the stratosphere, and the top of the boundary layer is set at either 850 or 700 hPa. The winter and summer lapse rate and PV gradient profiles in these runs are displayed and compared with the SD run in Figs. 6 and 7. To illustrate the role of the radiative–convective forcing, we also define a RCE state PV gradient, where

$$\frac{\partial q_e}{\partial y} = \beta + f_0 \frac{\partial}{\partial p} \left(\frac{\partial \theta_e}{\partial y} / \frac{\partial \bar{\theta}_e^{xy}}{\partial p} \right). \quad (6)$$

The vertical distribution of the RCE state PV gradient is also plotted in Figs. 6 and 7. By comparing these simulations, the influences of the radiative–convective forcing, boundary layer forcing, and baroclinic eddy can be distinguished.

Comparison of the RCE state PV gradient in Fig. 6b (which is the same as in Fig. 6d) and Fig. 7b shows that in both summer and winter the RCE state PV gradient in the moist adiabatic state is much weaker than in the “dry adiabatic” state. One important reason is that in the moist adiabatic state, the vertical variation of the lapse rate is considered. As shown in Figs. 2b and 2c, in a moist adiabatic state, the upper-level lapse rate is close to the dry adiabatic lapse rate, while the stratification in lower levels is more stable because the atmosphere there is more moist and warmer. Thus, in the moist adiabatic state, the stratification becomes less stable with height, which weakens the contribution of the baroclinic term to the PV gradient. At some levels (e.g., around 600 hPa in winter), it even acts against β slightly and results in a weaker PV gradient there.

As the depth of the boundary layer varies, the most obvious variation occurs in the 2D runs and during the summertime of the 3D runs, in which the locations of the local maximum stratification and the interior minimum PV gradient all move up as the boundary layer becomes deeper. In these situations, taking the SD run as an example, although the temperature gradient in the lower level is not modified as strongly as in winter, the stratification at the top of the boundary layer becomes strongly stable as shown in Fig. 6a, which is a feature of the well-mixed boundary layer. Thus, at the top of the boundary layer, the isentropic slope is greatly reduced compared with its neighboring levels, which can efficiently offset β . However, different from the PV homogenization by eddy mixing, the strongly stable stratification can even result in a negative PV gradient, as shown in Fig. 6b. The role of the stratification is more clearly seen in Fig. 7, in which we find that despite the seasonal forcing, the robust stratification distribution results in a robust PV structure through the whole year. The sensitivity study to the depth of the boundary layer shows that although the radiative–convective forcing can affect the PV structure, the boundary layer thermal forcing is most responsible for the weak interior PV gradient in the 2D runs and during the summertime of the 3D runs. In these situations, the location of the smallest PV gradient always stays above the top of the boundary layer and moves with the depth of the boundary layer.

During the wintertime of the 3D runs, as shown in Figs. 6a and 6c, the lapse rate shows different vertical distribution from summer or the 2D runs. The strong stabilization of the lower level stratification is mainly attributed to the baroclinic eddies and its vertical distribution does not show obvious variation with the depth of the boundary layer. Combined with this, as shown in Fig. 5a, the lower-level meridional temperature gradient is strongly reduced, especially near the steering level,

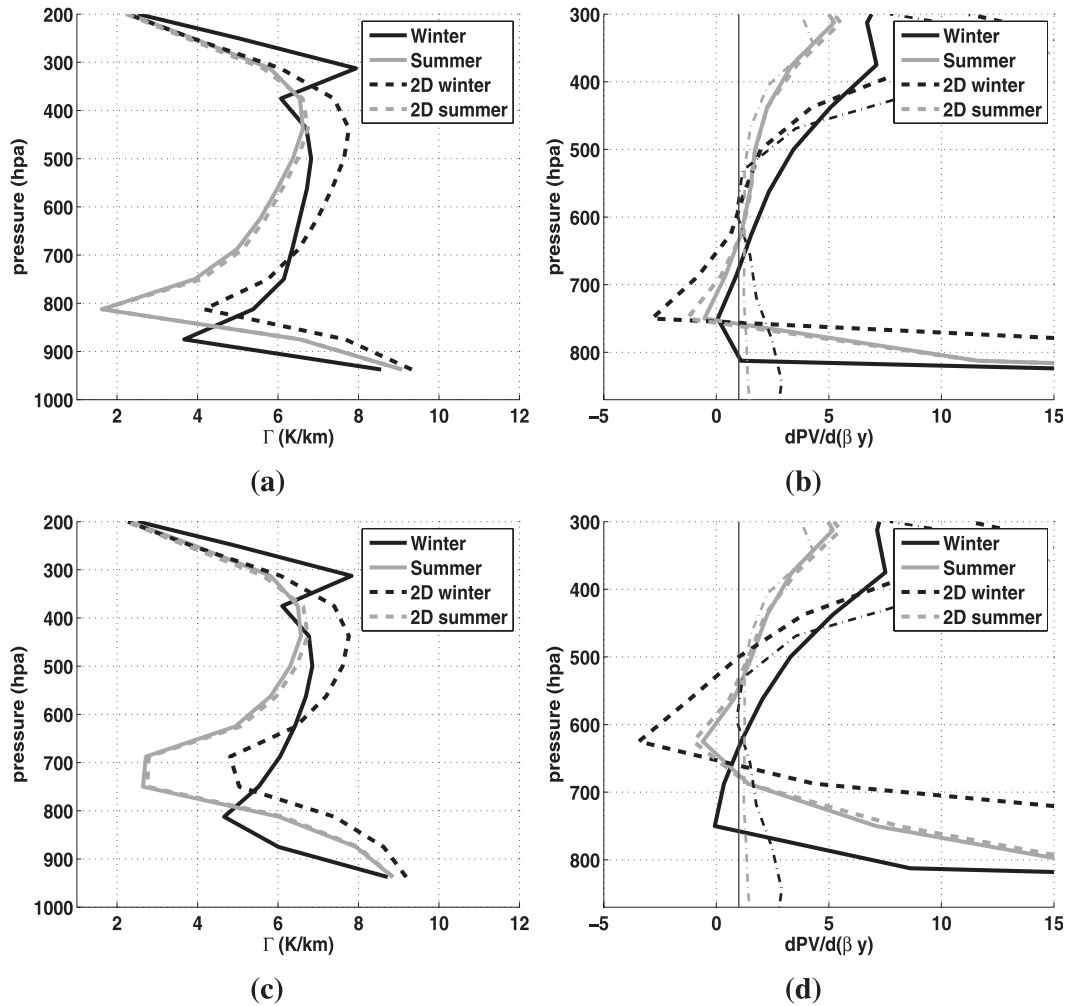


FIG. 6. Vertical distribution of the (a),(c) lapse rate (K km^{-1}) and (b),(d) meridional PV gradient at the center of the channel (normalized with β) averaged in the winter [January–March (JFM)] and summer [July–September (JAS)] seasons in the 2D and 3D runs with $p_{bl} = 850$ and 700 hPa, respectively. In (b) and (d), the RCE state PV gradient averaged in winter (black dot–dashed curves) and summer (gray dot–dashed curves) seasons is also plotted. The PV gradient β is marked by a thin solid line.

where the eddy mixing is strongest. Thus, as shown in Fig. 6b, the winter PV gradient around the steering level is efficiently homogenized, which, as suggested in Zurita and Lindzen (2001), is also a necessary condition for baroclinic eddies to neutralize the mean flow (Bretherton 1966). The same PV homogenization is also clearly seen in Fig. 6d.

The adjustment and vertical variation of the stratification play an important role in maintaining the robust PV structure through the whole year. Baroclinic eddies always act to keep a robust isentropic slope distribution. Near the boundary layer, especially at the top of a well-mixed boundary layer, the strongly stable stratification there offsets the planetary PV gradient β and also acts to keep a weak PV gradient there. The vertical distribution

of the moist adiabatic lapse rate can affect the contribution of the isentropic slope to the PV gradient as well.

We want to point out that a characteristic temperature profile of a well-mixed boundary layer (e.g., the summer lapse rate in Fig. 6a) is always seen in the daytime temperature soundings but is not clearly observed in the time- and space-averaged temperature profile, as the atmospheric boundary layer itself has strong spatial and time variations (e.g., the boundary layer temperature profile over land and ocean may differ and the depth of the well-mixed boundary layer over land has a strong diurnal cycle). However, our model results show that at the top of a well-mixed boundary layer, where the stratification is strongly stable, a weak PV gradient can be observed.

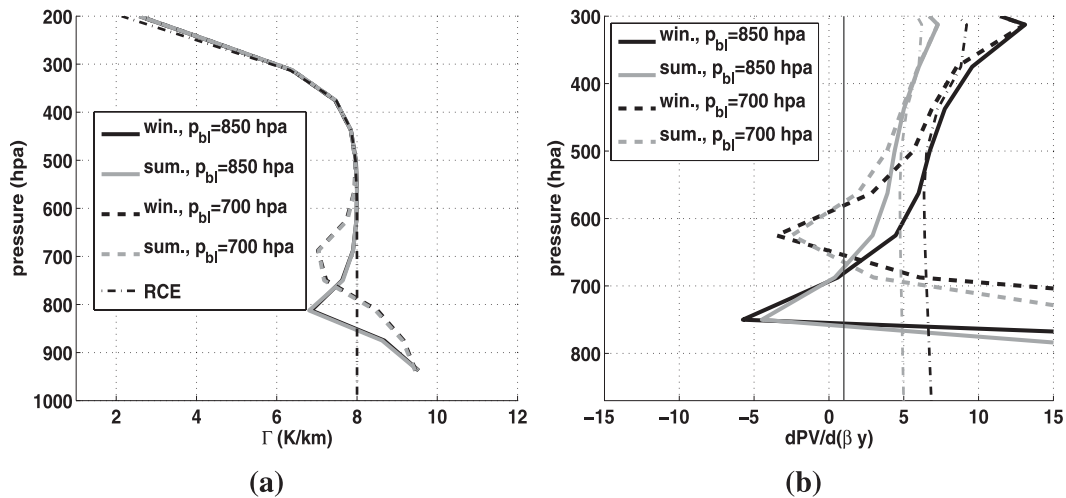


FIG. 7. Vertical distribution of the (a) lapse rate (K km^{-1}) and (b) meridional PV gradient at the center of the channel (normalized with β) averaged in the winter and summer seasons in the 2D “dry adiabatic” runs with $p_{bl} = 850$ and 700 hPa. In (b), the RCE state PV gradient averaged in winter (black dot-dashed curves) and summer (gray dot-dashed curves) is also plotted. The PV gradient β is marked by a thin solid line.

5. Sensitivity to the time scale of the external forcing

To investigate the time scale separation between the baroclinic adjustment and the external forcing, in this section sensitivity studies are carried out by varying the time scale of the external forcing. A modified time variable t_{date} (day) is used in the sensitivity studies to indicate the phase of the external forcing, where

$$t_{\text{date}} = \frac{t}{T_{\text{year}}} \times 365 \quad (7)$$

and T_{year} is the variation period of the external forcing. In the SD run, the seasonal behavior of the atmospheric flow is driven by the external forcing with $T_{\text{year}} = 1$ yr. A fast Fourier transform (FFT) analysis shows that the eddy activity in the SD run has a lifetime scale of 4–5 days (results not shown here). With these two time scales, the seasonal behavior of the eddy and the mean flow is clearly divided into four time intervals. How do these seasonal patterns depend on T_{year} ? Can the quick baroclinic adjustment be a good assumption when applied to the midlatitude climate? These are the questions that will be discussed in this section.

Compared to the SD run, a group of tests are carried out by assuming $T_{\text{year}} = 5, 2, 1/2,$ and $1/5$ yr, respectively. In all of these runs, T_g and θ_e vary periodically with t_{date} , as in Figs. 1 and 2c. Still, we start the model on 1 January and let the model reach an equilibrium state under the wintertime forcing. Then we turn on the seasonal variation of the external forcing and integrate the model for

15 forcing periods. Statistics are obtained from the last 10 forcing periods.² Their energy evolutions as a function of t_{date} are plotted in Fig. 8. For convenience, “month” and “date” are still used for t_{date} to describe the phase of the external forcing.

As shown in Fig. 8, when the external forcing period is long enough (more specifically, when the forcing period is longer than one year), the zonal flow and the eddy activity show characteristics similar to those of the SD run: a short eddy spinup period, a quasi-equilibrium “winter” for MPE, a relatively longer eddy decay period from late winter to late “spring,” and an eddy inactive “summer.” Eddies begin growing to finite amplitude earlier and the mean flow reaches the quasi-equilibrium state earlier for longer forcing period runs. As we will show later in this section, this is primarily because the eddy growth rate and the spinup time scale are mainly dynamically determined. Then in the longer forcing period runs, eddies have more time to grow to finite amplitudes. Even though eddies begin to spin up at different time, during their decay period the eddy energy decaying relative to t_{date} is similar. When $T_{\text{year}} = 5$ yr, at the end of the eddy decaying state, as the eddy energies become weak, instead of keeping the quasi-equilibrium state, MPE shows a temporary increase and decays only later to smaller values.

² For the experiment with $T_{\text{year}} = 1/5$ yr, the atmospheric flow shows stronger year-to-year variations than other experiments. However, their seasonal pattern is still similar and the results averaged over the last 10 forcing periods are basically the same as the results averaged over more forcing periods.

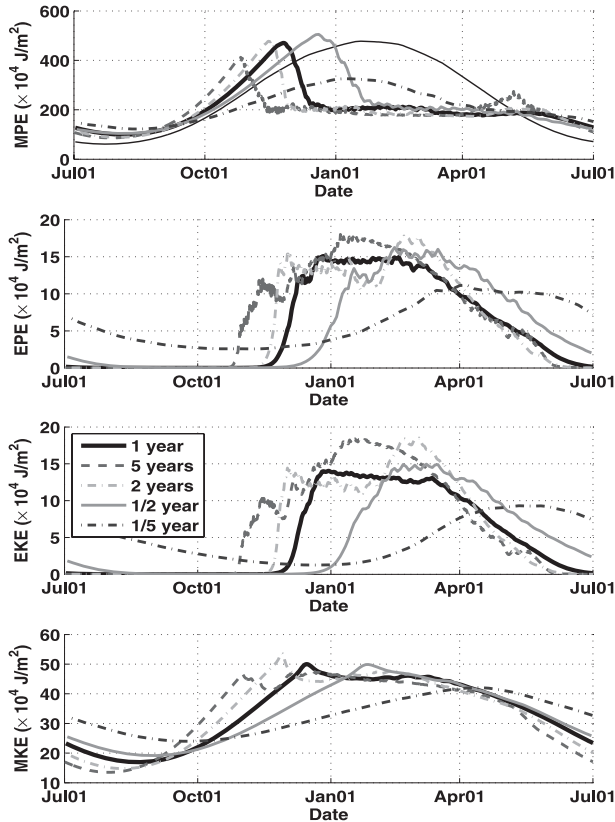


FIG. 8. Seasonal variation of domain averaged (a) MPE, (b) EPE, (c) EKE, and (d) MKE averaged over the last 10 forcing cycles as a function of t_{date} , when the period of the external forcing is changed from 1 to 5, 2, $\frac{1}{2}$, and $\frac{1}{5}$ yr. In (a), the seasonal evolution of the RCE state MPE is also plotted in thin black curve. Units for energy are 10^4 Joules per square meter.

When the external forcing is quickly varying (i.e., when $T_{\text{year}} = \frac{1}{2}$ yr), the seasonal pattern of the baroclinic eddies is less obvious. When $T_{\text{year}} = \frac{1}{5}$ yr, the eddy and the zonal flow do not show any characteristic seasonal pattern like those in the SD run. The MPE varies almost in proportion to the external forcing. EPE and EKE as well as MKE vary with MPE but with a lag of 15–30 days (which is 75–150 forcing days for t_{date}). The maximum eddy energies are smaller than the SD run, while eddies still have finite-amplitude activity during summer.

In all of these runs, the eddy activity has a characteristic life period of 4–5 days (results not shown); thus, the different seasonal behaviors of the atmospheric flow in these runs are purely due to the changing of T_{year} . The seasonality of the energies depends on the time scale of the external forcing. A quasi-equilibrium winter exists only under the slowly varying external forcing. When the external forcing varies quickly (e.g., $\frac{1}{5}$ -yr period), we will not see any other response time scales. From Figs. 4 and 8, we see that under slowly varying seasonal

forcing, the seasonal behavior of eddy activity exhibits two time scales: a spinup time scale, which is usually less than 30 days, and a spindown time scale, which can be as long as 2–3 months in the SD run. More analyses are made to investigate the factors that determine these two time scales.

a. Spinup time scale

Eddy growth/decay rates, defined as $(1/EKE)(dEKE/dt)$, are plotted in Fig. 9a as a function of t_{date} for different T_{year} runs. Except for the $T_{\text{year}} = \frac{1}{5}$ -yr run, in all the other experiments eddy growth rate/decay rates show more features.

Eddy activity experiences a fast exponentially growing period in the middle of fall or early winter. The growth rates in this period are also plotted as a function of model day in Fig. 9b, in which the maximum growth rate day is labeled as day 0. We find that their fast growing states are all maintained for around 30 days; after reaching the maximum growth rate, their growth rates all drop down quickly in around 10 days, which is consistent with the previous eddy life cycle studies and suggests that the increasing nonlinear interactions act to prevent further eddy growth as their amplitudes grow. As the external forcing time scale increases, as shown in Fig. 9a, eddies begin to spin up earlier but with a lower maximum growth rate and maintain a longer period of fast growth, as shown in Fig. 9b. The relation between the largest growth rate and the MPE during the fastest growing period is also plotted in Fig. 9c. Eddy growth rate is correlated with MPE in a way consistent with the linear instability theory. The growth rate gets stronger with MPE. In the quasi-equilibrium state, the eddy growth/decay rate oscillates around the zero line until spring when eddies begin decaying. The eddies decay with a rate weaker than their growth rate but can last longer.

From Fig. 9 we find that eddy behavior in their growing state shows characteristics similar to those predicted by linear instability theory. Their spinup time scale is mainly dynamically determined. When $T_{\text{year}} = \frac{1}{5}$ yr, eddies do not have an obvious spinup or spindown period, in which the eddy growth/decay rate follows the variation of the external forcing and MPE with a roughly 10 days' delay (around 50 days for t_{date}).

b. Spindown time scale

Under the slowly varying external forcing, one characteristic during the eddy spindown period is that even though eddy activity decays, MPE stays at a relatively constant value through most of the period. Thus, we start our analysis from the MPE energy budget.

In our modified QG model, the total balance equation of MPE is

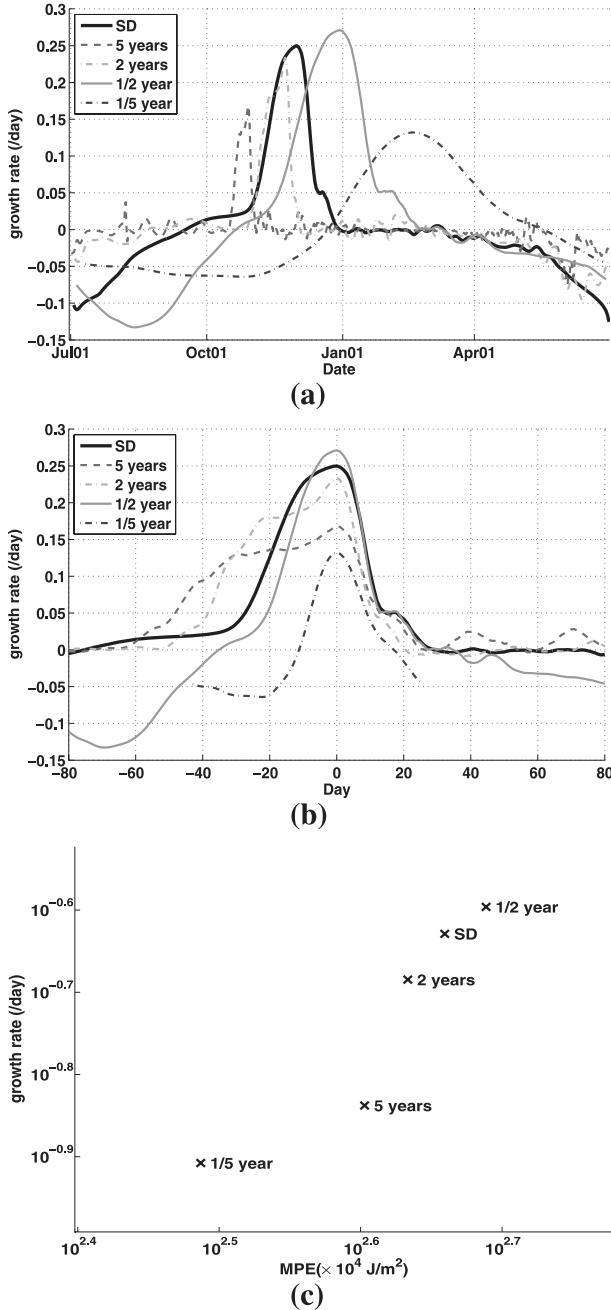


FIG. 9. (a) Seasonal variation of the eddy growth/decay rate (day^{-1}) as a function of t_{date} ; (b) evolution of eddy growth rate (day^{-1}) as a function of model day during the eddy spinup period, where day = 0 is the day that eddy growth rate is largest; and (c) variation of the eddy growth rate in the eddy spinup period as a function of MPE for different T_{year} .

$$\frac{d}{dt} \text{MPE} = G_{\text{MPE}}(Q) - C(\text{MPE}, \text{EPE}) - C(\text{MPE}, \text{MKE}) + G_{\text{MPE}}(\sigma). \quad (8)$$

In our model,

$$G_{\text{MPE}}(Q) = \int \sigma([T] - \bar{T}^{xy})([Q] - \bar{Q}^{xy}) dm \quad (9)$$

is the generation of MPE by differential heating Q , which has two components: the generation of MPE by radiative-convective heating $G_{\text{MPE}}(Q_{\text{rad}})$ and by boundary layer thermal diffusion $G_{\text{MPE}}(Q_{\text{dif}})$. Also,

$$C(\text{MPE}, \text{MKE}) = - \int \frac{R}{p} [\omega][T] dm \quad (10)$$

indicates the conversion rate from MPE to MKE through the zonal mean meridional overturning circulation. One difference between our model and the traditional QG model is that our stratification is allowed to vary with time. Thus, in the balance equation of MPE, there is another generation term of MPE by changing the flow stratification,

$$G_{\text{MPE}}(\sigma) = \int \left(\frac{d}{dt} \sigma \right) \frac{c_p}{2} ([T] - \bar{T}^{xy})^2 dm, \quad (11)$$

where the tendency term $(d/dt)\sigma$ is determined by our stratification tendency [Eq. (A1)].

In the 3D simulation, the conversion rate from MPE to EPE through eddy poleward heat transport down the zonal mean temperature gradient, which is

$$C(\text{MPE}, \text{EPE}) = -c_p \int \sigma [v^* T^*] \frac{\partial [T]}{\partial y} dm, \quad (12)$$

is another important term in the MPE balance equation.

Time evolutions of these energy flux terms are plotted in Fig. 10, from which we find that during the eddy spinup period, from t_0 to t_1 , $C(\text{MPE}, \text{EPE})$ also increases exponentially to reduce MPE. As the lower-level stratification is strongly stabilized by the baroclinic eddies, $G_{\text{MPE}}(\sigma)$ also becomes an important sink for MPE. This is the only period during the whole year that $G_{\text{MPE}}(\sigma)$ plays an important role in changing MPE. These two factors work together, causing the quick decrease of MPE. In this time interval, $G_{\text{MPE}}(Q)$ also changes steeply, which, as shown in Fig. 10b, mainly comes from the contribution of $G_{\text{MPE}}(Q_{\text{dif}})$. As shown in Fig. 5a, the strong variation of the temperature structure plays an important role. As the eddy spins up, the meridional temperature gradient is strongly reduced around the steering level, while near the surface, because of the surface drag, a strong surface temperature gradient still remains. Such a dramatic variation on the vertical structure of the temperature strongly enhances the boundary layer vertical diffusion.

After t_1 , MPE reaches a quasi-equilibrium state, in which $G_{\text{MPE}}(Q)$ and the eddy transport term are the two

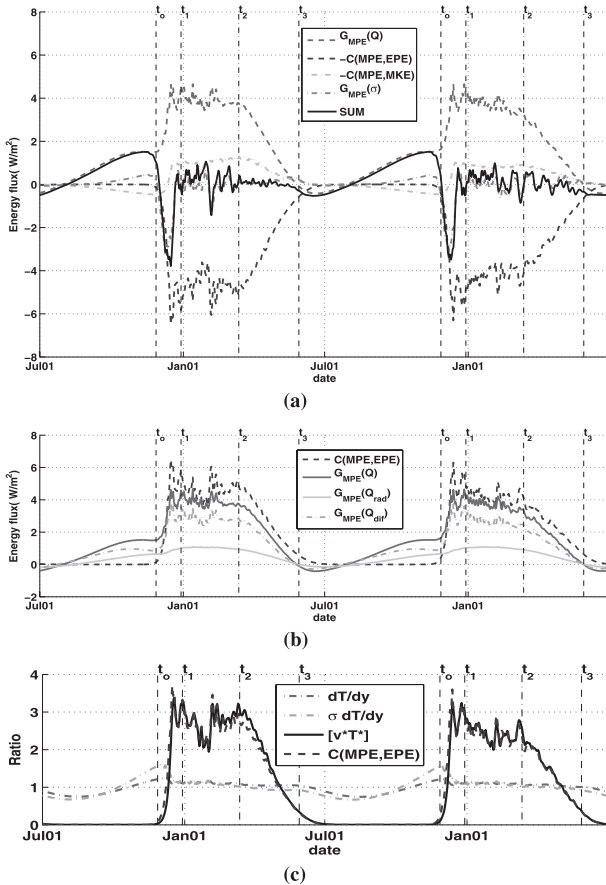


FIG. 10. Time evolution of (a) each term in MPE balance equation; (b) $C(\text{MPE}, \text{EPE})$, $G_{\text{MPE}}(Q)$, and its two components: $G_{\text{MPE}}(Q_{\text{rad}})$ and $G_{\text{MPE}}(Q_{\text{dif}})$; and (c) normalized domain averaged $\partial[T]/\partial y$, $\sigma[\partial(T)/\partial y]$, and $[v^*T^*]$ compared with $C(\text{MPE}, \text{EPE})$ in two seasonal cycles in the SD run. Units for energy fluxes are watts per square meter in (a) and (b). The eddy spinup, spindown, and MPE quasi-equilibrium periods are marked by t_0 , t_1 , t_2 , and t_3 .

dominant factors that maintain MPE, with $C(\text{MPE}, \text{MKE})$ playing a minor role in increasing MPE given the fact that the zonal flow has a Ferrel cell circulation in this period. As shown in Fig. 10b, these two terms are comparable and highly correlated from t_1 to t_3 . A close look at the two components of $G_{\text{MPE}}(Q)$ also shows that $G_{\text{MPE}}(Q_{\text{rad}})$ and $G_{\text{MPE}}(Q_{\text{dif}})$ both act to increase MPE, with $G_{\text{MPE}}(Q_{\text{dif}})$ having the larger contribution, which is consistent with Zhang et al. (2009). The boundary layer thermal forcing acts as a strong source of the lower-level baroclinicity by dragging the air temperature near the surface close to the underlying surface temperature.

Starting from t_2 , the external forcing as well as $G_{\text{MPE}}(Q)$ begin to decrease. To balance it, the eddy transport term also needs to decrease. The time evolution of the different components in $C(\text{MPE}, \text{EPE})$ is also investigated. As shown in Fig. 10c, along with the robust MPE and the

slightly varying thermal structure of the mean flow, the decreasing $C(\text{MPE}, \text{EPE})$ mainly indicates a decay of eddy poleward heat flux and eddy energies. During the eddy active time interval, it is the eddy heat fluxes that are highly sensitive to the variation of the external forcing.

At t_3 , when the underlying surface and the target state temperature gradients become smaller than the quasi-equilibrium state temperature gradient, as indicated in Figs. 3a and 5a, both $G_{\text{MPE}}(Q_{\text{rad}})$ and $G_{\text{MPE}}(Q_{\text{dif}})$ change sign and start acting to reduce the atmospheric temperature gradient. Then, as shown in Fig. 10b, the quasi-equilibrium state cannot be maintained any more and begins to decrease. After t_3 , eddies become inactive and the differential heating is the dominant factor that determines MPE evolution.

From the maintenance of MPE during the seasonal cycle we find that the decay of eddy activity is primarily the eddy response to the decreasing differential heating, which implies that the decay time scale is mainly determined by the external forcing. This is also indicated by Figs. 8b and 8c, in which, when we vary the time scale of the external forcing, the eddies in the long forcing period runs display a similar decay behavior as a function of t_{date} .

6. Summary and discussion

Baroclinic eddy equilibration under a Northern Hemisphere-like seasonal forcing is studied using a β -plane multilayer QG channel model, in which seasonal variation of the surface temperature is specified as the lower boundary condition to act on the atmospheric flow through the boundary layer processes and the radiative-convective heating. The seasonal forcing on the atmospheric stratification is also included in our study. Under the time-varying external forcing, the eddy and mean flow seasonal behaviors can be clearly divided into four time intervals: an eddy inactive time interval during the summer, an eddy spinup time interval starting from midfall and lasting less than one month, and a quasi-equilibrium time interval for MPE from late fall to late spring, with a spindown time interval for the eddy activity from late winter to late spring. During the quasi-equilibrium time interval for MPE, in spite of the strong varying of the external forcing, MPE always stays at a relatively constant value and the mean flow thermal structure only varies slightly. In this time interval, the baroclinic eddy is the dominant dynamical process and a baroclinic adjustment scenario suggested in Stone (1978) and Lindzen and Farrell (1980) does occur, in which the mean flow has a preferred equilibrium state and it is the eddy heat fluxes that are highly sensitive to the external forcing and act to maintain the relatively

robust mean flow thermal structure. The decay time scale of the eddy activity in this time interval is therefore determined by the variation of the external forcing.

Although the eddy activity has strong seasonal variation in our simulation, the zonal mean flow PV structure is robust all year, just as observed in the real atmosphere (Kirk-Davidoff and Lindzen 2000; Zurita-Gotor and Lindzen 2007). Our study shows that baroclinic eddies are able to maintain a robust PV structure under the seasonal forcing, but they are not the only possible mechanism. During winter, when the mean flow adjustment by the baroclinic eddies is dominant, the robustness of the PV gradient is consistent with the previous equilibrium studies (Stone and Branscome 1992; Solomon and Stone 2001b; Zurita-Gotor 2008, etc.) and indicates that when baroclinic eddies are strong enough, the conclusions obtained in these equilibrium studies will hold under a seasonally varying external forcing. However, in summer when the baroclinic eddy is too weak to play any role, the slightly varying PV structure indicates that other physical processes can also be responsible for the observed PV structure. Our model results show that the boundary layer thermal forcing can help maintain the small PV gradient in the lower troposphere by modifying the stratification there.

Our study emphasizes the importance of the stratification adjustment for the robustness of the PV structure. By using a model with better vertical resolution, we showed that vertical variation of the stratification caused by baroclinic eddies and boundary layer thermal forcing makes an important contribution to the robust PV structure, which is a factor historically overlooked from the use of the two-layer model. In addition to the stratification adjustment by baroclinic eddies as suggested in Stone (1972), Gutowski (1985), and Schneider (2004, 2007), the local maximum in the stratification at the top of a boundary layer can act against β and result in an interior minimum PV gradient. The vertical variation of the moist adiabatic state lapse rate, which is less stable with height in the troposphere, can act to weaken the PV gradient as well.

The robustness of the mean flow and the baroclinic eddy seasonal behavior as well as the “quick baroclinic adjustment” assumption is further investigated by artificially varying the period of the external forcing. The separation into four distinct time intervals is robust under a slowly varying seasonal forcing. However, when the variation period of the external forcing is reduced from 1 to $\frac{1}{2}$ yr, this feature becomes less obvious. When the forcing period is further reduced to $\frac{1}{5}$ yr, this feature totally disappears. In all of these experiments, the eddy lifetime scale is always around 5 days, which is much shorter than the external forcing variation period even

for the $T_{\text{year}} = \frac{1}{5}$ -yr run. However, the time scale separation between the baroclinic adjustment and the external forcing in these two runs is not obvious. This confirms that the time scale of the baroclinic adjustment is longer than the eddy life cycle time scale.

Our SD run and sensitivity studies reveal the conditions under which baroclinic adjustment can be applied to the midlatitude climate. Our sensitivity studies show that baroclinic adjustment is valid only for external forcing periods one year and longer, for which the quick baroclinic adjustment is a good assumption. Our SD run shows that the baroclinic adjustment can be observed in the Northern Hemisphere only from late fall to late spring. To test how these conditions work in the real atmosphere, the seasonal variation of the MPE is calculated using National Centers for Environmental Prediction (NCEP)–National Center for Atmospheric Research (NCAR) daily reanalysis data. One difficulty in comparing our model results with observations is that MPE highly depends on the area (the baroclinic zone) over which it is defined. As indicated in the definition of MPE in Eq. (3), $\text{MPE} \sim (c_p/2)\sigma\langle d[T]/dy \rangle^2 L_{\text{MPE}}^2$, where L_{MPE} is the width of the baroclinic zone over which MPE is defined and $\langle d[T]/dy \rangle$ is the characteristic meridional temperature gradient in the baroclinic zone. Here we estimate the MPE defined over four regions: the whole Northern Hemisphere; 90° – 30°N , where the baroclinic eddy activity is confined; 65° – 25°N , where the transient eddies are most active; and 70° – 40°N , where the stationary eddies are strongest (Peixoto and Oort 1992). The annual patterns of MPE defined over these four regions are displayed in Fig. 11.

Similar to our model results, in spite of the variation of the external forcing, the MPE defined in these regions always stays at a relatively constant value in winter. This tendency is more obvious when the MPE is calculated over the extratropical region. In Figs. 11b and 11d, a peak of the MPE appears in midfall, and then the MPE also stays in a quasi-equilibrium state with a smaller magnitude from late fall to midspring. In summer, the quasi-equilibrium state for MPE cannot be maintained and MPE becomes much weaker with the minimum occurring in midsummer. These features are consistent with our model results.

Comparison with observations also raises questions as to the role of the stationary eddies in midlatitude climate. In our model, we only apply a zonally symmetric external forcing, which neglects the longitudinal variation of the underlying surface (i.e., land–sea contrast) in the Northern Hemisphere, and all the eddies in our model are transient eddies. However, the stationary and transient eddies are also found to be highly correlated in the midlatitudes (Stone and Miller 1980). Thus, to better apply

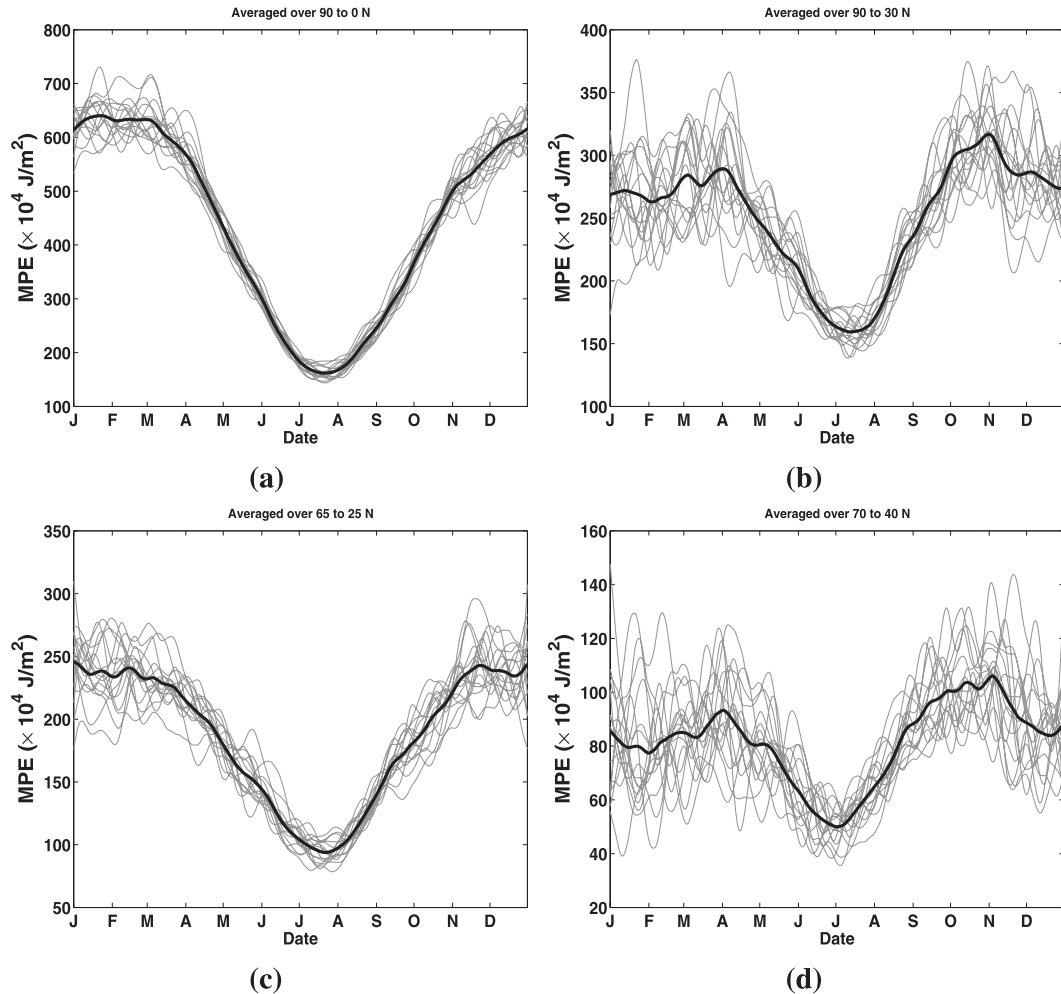


FIG. 11. Seasonal variations of MPE averaged over (a) the NH, (b) 90° – 30° N, (c) 65° – 25° N, and (d) 70° – 40° N using the NCEP–NCAR daily reanalysis data. Gray curves are the 10-day running mean MPE seasonal behavior in each of the years between 1985 and 2000; black curves are the MPE averaged over these years.

our model results to the real atmosphere, the relative roles of transient and stationary eddies in the eddy–mean flow interactions in the Northern Hemisphere require more study. In our channel model, the effect of the tropic forcing is also neglected. The extent to which it can affect the seasonal cycle of MPE is still not clear.

Another possible inconsistency when comparing our model results with the midlatitude climate is that the eddy energy in summer in our model is too weak compared to observations. Peixoto and Oort (1992) showed that the observed EKE averaged over the summer season decreases to half of the wintertime magnitude. Trenberth (1991) showed that the observed heat and momentum fluxes by synoptic eddies in July can be as low as one-tenth of their values in January. Although the observed eddy activity is much weaker in summer, it still makes finite-amplitude contributions. Thus, in the real

atmosphere, there is no such clear eddy spinup time interval as in our model. This is also reflected in Fig. 11, in which MPE does not have such an obvious peak in late fall as in our model.

A plausible source for EPE that is omitted in our model is the release of latent heat, especially in summer when the moisture effect is more important. Stone and Salustri (1984) defined a generalized Eliassen–Palm flux by including the large-scale eddy forcing of condensation heating and showed that, in the midlatitudes, including the condensation effect leads to much stronger eddy forcing, especially in summer. Previous studies indicate that moisture has competing effects on the midlatitude baroclinic eddies. It serves as a source of the eddy available potential energy (Emanuel et al. 1987); on the other hand, the increased moisture can increase the extratropical stratification (Frierson et al. 2006; O’Gorman

and Schneider 2008; Schneider et al. 2010), which may weaken the eddy activity. Some studies (Oort and Peixoto 1983; Gutowski et al. 1992; Davis et al. 1993; Chang et al. 2002) indicate that the former effect may dominate the latter one for the current climate. In our dry model, only the effect of the moisture on the horizontal averaged stratification is included, which acts to suppress the eddy activity by stabilizing the lower-level flow. The radiative–convective forcing in our model through the Newtonian cooling acts to damp the eddy activity in the eddy energy cycle, which may be opposite to the net effect of the moisture on the baroclinic eddies and result in much weaker eddy activity in summer. This is also a limitation for all the dry models. Moist baroclinic eddy equilibration under the seasonal forcing will be an interesting future topic.

Acknowledgments. This study is part of the first author’s thesis work at MIT. We thank Richard Lindzen, Alan Plumb, and Raffaele Ferrari for discussions and thank Paul O’Gorman for his comments on an earlier draft of this paper. We thank the two anonymous reviewers for their comments, which led to an improvement of the manuscript. Both authors were supported by the Office of Science (BER), U.S. Dept. of Energy, Grant DE-FG02-93ER61677, and the Goddard Institute for Space Studies, under NASA Cooperative Agreement NNG04GF12A. The first author was also supported by the National Natural Science Foundation of China under Grant 40730953.

APPENDIX

Model Description

In our β -plane multilevel quasigeostrophic channel model, the variables are defined in gridpoint space. The horizontal resolution of the model is 330 km in both zonal and meridional directions. The model has 17 equally spaced levels. As shown by Solomon (1997) and Solomon and Stone (2001a), this horizontal and vertical resolution is appropriate to simulate the eddy dynamics. In addition, an FFT filter is used on the streamfunction to remove the smallest-scale eddies.

a. Governing equations

In this model, the potential vorticity equation, including diabatic heating and boundary layer dissipation, is integrated:

$$\frac{\partial q}{\partial t} = -J(\psi, q) - f_0 \frac{\partial}{\partial p} \frac{QR}{spc_p} + \mathbf{k} \cdot \nabla \times \mathbf{F},$$

where p is the pressure, f_0 is the Coriolis parameter at the center of the channel, R is the ideal gas constant, c_p is the specific heat of the air, $s = -(R/p)(p/p_0)^{R/c_p}(\partial/\partial p)\bar{\theta}^{xy}$ is the static stability parameter, and ψ is the geostrophic streamfunction; also, \mathbf{F} denotes the frictional dissipation and the heating term Q has two contributors: the radiative–convective heating Q_{rad} and the thermal diffusion in the boundary layer Q_{dif} . Potential vorticity $q = \nabla^2 \psi + f_0 + \beta_y + (\partial/\partial p)(f_0^2/s)(\partial\psi/\partial p)$.

One important difference between this model and traditional QG models is that the horizontally averaged potential temperature and static stability, instead of being specified, are allowed to evolve with time according to the equation

$$\frac{\partial \bar{\theta}^{xy}}{\partial t} = -\frac{\partial}{\partial p} \overline{\omega^* \theta^{*xy}} + \frac{\overline{Q_{\text{rad}} + Q_{\text{dif}}^{xy}}}{c_p} \left(\frac{p_0}{p}\right)^{R/c_p}, \quad (\text{A1})$$

where $\overline{(\dots)^{xy}}$ means averaged horizontally and the asterisk indicates the eddy component of the variable. This tendency equation is derived from the horizontally averaged thermodynamic equation and is exact except that the heating associated with the vertical heat flux by the zonal mean flow is neglected. As shown by Gutowski (1983), this is a reasonable approximation in midlatitudes. Thus, in our model the thermal stratification is maintained by the vertical eddy heat flux and the radiative–convective heating in the free atmosphere and by the vertical eddy heat flux, radiative–convective heating, and thermal diffusion in the boundary layer. As shown by Gutowski (1985), the interaction between the vertical eddy heat flux and the stratification, which is neglected in conventional QG theory, plays an important role in baroclinic adjustment. Since we still use horizontal uniform stratification, adding Eq. (A1) does not break the QG scaling. The horizontal variation of the stratification and the relevant dynamic feedback are still assumed to be small and are neglected, which, as shown in observations and numerical studies (Zurita-Gotor and Vallis 2009), is a good approximation for midlatitude climate and baroclinic adjustment. In addition, in the quasi-equilibrium state, where the stratification has tiny variations with time, the model behavior is similar to the traditional QG model with time-invariant stratification, which has been confirmed by Solomon and Stone (2001a) and Zurita-Gotor and Vallis (2009).

b. Radiative–convective heating

Radiative–convective heating in this model is parameterized by the Newtonian cooling form:

$$Q_{\text{rad}} = c_p \frac{T_e - T}{\tau_r}, \quad (\text{A2})$$

where T_e is the atmospheric temperature in the radiative–convective equilibrium state corresponding to the specified surface temperature and $\tau_r = 40$ days is the relaxation time scale. Note that T_e (as well as θ_e), as described in section 2, is specified to vary seasonally to match the underlying surface temperature.

c. Thermal diffusion in the boundary layer

The surface heat exchange between atmosphere and the underlying surface is represented by the linearized bulk aerodynamic drag formula:

$$F_{\text{sh}} = -C_{\text{dt}} c_p \rho_s (\theta_{\text{air}} - \theta_g), \quad (\text{A3})$$

where $C_{\text{dt}} = C_{\text{surface}} |\mathbf{v}_s|$ is the drag coefficient. In this study, C_{dt} is chosen to be constant, and 0.03 m s^{-1} is taken as its standard value. The seasonal variation of the surface potential temperature θ_g is specified in section 2. We assume that the first model level is a well-mixed layer so that the surface air potential temperature θ_{air} is equal to the potential temperature at the first level, which is 32 hPa above the surface.

Above the surface, the vertical turbulent heat flux in the boundary layer is parameterized in the diffusive form:

$$F_{\text{sh}} = \nu_s(p) c_p \rho^2 g \frac{\partial \theta}{\partial p}. \quad (\text{A4})$$

The vertical distribution of the diffusion coefficient is set to be

$$\nu_s(p) = \mu_s \left(\frac{p - p_{\text{bl}}}{p_0 - p_{\text{bl}}} \right)^3 \quad (\text{A5})$$

for $p \geq p_{\text{bl}}$, and $\nu_s(p) = 0 \text{ m}^2 \text{ s}^{-1}$ for $p \leq p_{\text{bl}}$, where $p_{\text{bl}} = 850$ hPa is the pressure at the top of the boundary layer and 5 is taken to be the default value for μ_s . Heating by thermal diffusion is calculated from the heat flux:

$$Q_{\text{dif}} = g \left(\frac{p}{p_0} \right)^{R/c_p} \frac{\partial F_{\text{sh}}}{\partial p}. \quad (\text{A6})$$

Here we want to point out that because of the vertical turbulent heat transport, the stratification in the boundary layer can be weak. However, this merely means the vertical temperature advection by the flow is small and the horizontal temperature advection in this case is dominant. Thus, the QG scaling still holds.

d. Frictional dissipation in the boundary layer

The parameterization of friction is analogous to thermal diffusion, $\mathbf{F} = g(\partial \tau_m / \partial p)$, where τ_m is the shear stress and is parameterized by a linearized bulk aerodynamic

drag at the surface and vertical diffusion in the boundary layer:

$$\tau_m = -C_{\text{dt}} \rho_s \mathbf{v} \text{ (surface)}, \quad (\text{A7})$$

$$\tau_m = \nu_m(p) \rho^2 g \frac{\partial \mathbf{v}}{\partial p} \text{ (boundary layer)}, \quad (\text{A8})$$

where $\mathbf{v} = (-\psi_y, \psi_x) = (u_g, v_g)$ and

$$\nu_m(p) = \mu_m \left(\frac{p - p_{\text{bl}}}{p_0 - p_{\text{bl}}} \right)^3 \quad (\text{A9})$$

for $p \geq p_{\text{bl}}$, and $\nu_s(p) = 0 \text{ m}^2 \text{ s}^{-1}$ for $p \leq p_{\text{bl}}$, where $\mu_m = 5 \text{ m}^2 \text{ s}^{-1}$ and C_{dt} is still chosen to be 0.03 m s^{-1} . In this study, only the shear stress by geostrophic component is considered.³

REFERENCES

- Barry, L., G. Craig, and J. Thuburn, 2000: A GCM investigation into the nature of baroclinic adjustment. *J. Atmos. Sci.*, **57**, 1141–1155.
- Bretherton, F., 1966: Critical layer instability in baroclinic flows. *Quart. J. Roy. Meteor. Soc.*, **92**, 325–334.
- Cehelsky, P., and K. Tung, 1991: Nonlinear baroclinic adjustment. *J. Atmos. Sci.*, **48**, 1930–1947.
- Chang, E., S. Lee, and K. Swanson, 2002: Storm track dynamics. *J. Climate*, **15**, 2163–2183.
- Chen, G., I. Held, and W. Robinson, 2007: Sensitivity of the latitude of the surface westerlies to surface friction. *J. Atmos. Sci.*, **64**, 2899–2915.
- Davis, C., M. Stoelinga, and Y. Kuo, 1993: The integrated effect of condensation in numerical simulations of extratropical cyclogenesis. *Mon. Wea. Rev.*, **121**, 2309–2330.
- Emanuel, K., 1988: Observational evidence of slantwise convective adjustment. *Mon. Wea. Rev.*, **116**, 1805–1816.
- , M. Fantini, and A. Thorpe, 1987: Baroclinic instability in an environment of small stability to slantwise moist convection. Part I: Two-dimensional models. *J. Atmos. Sci.*, **44**, 1559–1573.
- Frierson, D., I. Held, and P. Zurita-Gotor, 2006: A gray-radiation aquaplanet moist GCM. Part I: Static stability and eddy scale. *J. Atmos. Sci.*, **63**, 2548–2566.
- Gutowski, W. J., 1983: Vertical eddy heat fluxes and the temperature structure of the mid-latitude troposphere. Ph.D. thesis, Massachusetts Institute of Technology, 294 pp.
- , 1985: Baroclinic adjustment and the midlatitude temperature profiles. *J. Atmos. Sci.*, **42**, 1735–1745.
- , L. Branscome, and D. Stewart, 1992: Life cycles of moist baroclinic eddies. *J. Atmos. Sci.*, **49**, 306–319.
- Juckes, M., 2000: The static stability of the midlatitude troposphere: The relevance of moisture. *J. Atmos. Sci.*, **57**, 3050–3057.
- Kirk-Davidoff, D., and R. Lindzen, 2000: An energy balance model based on potential vorticity homogenization. *J. Climate*, **13**, 431–448.

³ As shown in Zhang (2009), including the influence of ageostrophic winds in the shear stress in the boundary layer, despite quantitative differences, will not influence the conclusions made in this study.

- Korty, R., and T. Schneider, 2007: A climatology of the tropospheric thermal stratification using saturation potential vorticity. *J. Climate*, **20**, 5977–5991.
- Lindzen, R. S., 1993: Baroclinic neutrality and the tropopause. *J. Atmos. Sci.*, **50**, 1148–1151.
- , and B. Farrell, 1980: The role of polar regions in global climate, and a new parameterization of global heat transport. *Mon. Wea. Rev.*, **108**, 2064–2079.
- O’Gorman, P., and T. Schneider, 2008: Energy of midlatitude transient eddies in idealized simulations of changed climates. *J. Climate*, **21**, 5797–5806.
- Oort, A. H., and J. P. Peixoto, 1983: Global angular momentum and energy balance requirements from observations. *Advances in Geophysics*, Vol. 25, Academic Press, 355–490.
- Pedlosky, J., 1970: Finite-amplitude baroclinic waves. *J. Atmos. Sci.*, **27**, 15–30.
- Peixoto, J. P., and A. H. Oort, 1992: *Physics of Climate*. Springer-Verlag, 520 pp.
- Schneider, T., 2004: The tropopause and the thermal stratification in the extratropics of a dry atmosphere. *J. Atmos. Sci.*, **61**, 1317–1340.
- , 2007: The thermal stratification of the extratropical troposphere. *The Global Circulation of the Atmosphere: Phenomena, Theory, Challenges*, T. Schneider and A. Sobel, Eds., Princeton University Press, 47–77.
- , and C. C. Walker, 2006: Self-organization of atmospheric macroturbulence into critical states of weak nonlinear eddy–eddy interactions. *J. Atmos. Sci.*, **63**, 1569–1586.
- , P. O’Gorman, and X. Levine, 2010: Water vapor and the dynamics of climate changes. *Rev. Geophys.*, **48**, RG3001, doi:10.1029/2009RG000302.
- Solomon, A. B., 1997: The role of large-scale eddies in the nonlinear equilibration of a multi-level model of the mid-latitude troposphere. Ph.D. thesis, Massachusetts Institute of Technology, 234 pp.
- , and P. H. Stone, 2001a: Equilibration in an eddy resolving model with simplified physics. *J. Atmos. Sci.*, **58**, 561–574.
- , and —, 2001b: The sensitivity of an intermediate model of the mid-latitude troposphere’s equilibrium to changes in radiative forcing. *J. Atmos. Sci.*, **58**, 2395–2410.
- Stone, P. H., 1972: A simplified radiative–dynamical model for the static stability of rotating atmospheres. *J. Atmos. Sci.*, **29**, 405–418.
- , 1978: Baroclinic adjustment. *J. Atmos. Sci.*, **35**, 561–571.
- , and J. Carlson, 1979: Atmospheric lapse rate regimes and their parameterization. *J. Atmos. Sci.*, **36**, 415–423.
- , and D. Miller, 1980: Empirical relations between seasonal changes in meridional temperature gradients and meridional fluxes of heat. *J. Atmos. Sci.*, **37**, 1708–1721.
- , and G. Salustri, 1984: Generalization of the quasi-geostrophic Eliassen–Palm flux to include eddy forcing of condensation heating. *J. Atmos. Sci.*, **41**, 3527–3536.
- , and L. Branscome, 1992: Diabatically forced, nearly inviscid eddy regimes. *J. Atmos. Sci.*, **49**, 355–367.
- Stull, R., 1988: *An Introduction to Boundary Layer Meteorology*. Kluwer Academic, 666 pp.
- Swanson, K., and R. T. Pierrehumbert, 1997: Lower-tropospheric heat transport in the Pacific storm track. *J. Atmos. Sci.*, **53**, 1533–1543.
- Trenberth, K., 1991: Storm tracks in the Southern Hemisphere. *J. Atmos. Sci.*, **48**, 2159–2178.
- Welch, W., and K. Tung, 1998a: Nonlinear baroclinic adjustment and wavenumber selection in a simple case. *J. Atmos. Sci.*, **55**, 1285–1302.
- , and —, 1998b: On the equilibrium spectrum of transient waves in the atmosphere. *J. Atmos. Sci.*, **55**, 2833–2851.
- Zhang, Y., 2009: Nonlinear equilibration of baroclinic eddies: The role of boundary layer processes and seasonal forcing. Ph.D. thesis, Massachusetts Institute of Technology, 266 pp.
- , P. Stone, and A. Solomon, 2009: The role of boundary layer processes in limiting PV homogenization. *J. Atmos. Sci.*, **66**, 1612–1632.
- Zurita, P., and R. Lindzen, 2001: The equilibration of short Charney waves: Implications for potential vorticity homogenization in the extratropical troposphere. *J. Atmos. Sci.*, **58**, 3443–3462.
- Zurita-Gotor, P., 2008: The sensitivity of the isentropic slope in a primitive equation dry model. *J. Atmos. Sci.*, **65**, 43–65.
- , and R. Lindzen, 2004: Baroclinic equilibration and the maintenance of the momentum balance. Part II: 3D results. *J. Atmos. Sci.*, **61**, 1483–1499.
- , and —, 2007: Theories of baroclinic adjustment and eddy equilibration. *The Global Circulation of the Atmosphere: Phenomena, Theory, Challenges*, T. Schneider and A. Sobel, Eds., Princeton University Press, 22–46.
- , and G. Vallis, 2009: Equilibration of baroclinic turbulence in primitive equation and quasi-geostrophic models. *J. Atmos. Sci.*, **66**, 837–863.